HEFAT2014
10th International Conference on Heat Transfer, Fluid Mechanics and Thermodynamics
14 - 16 July, 2014, Orlando, Florida
Paper No: 1569879071

Heat Transfer Modeling of Laser Cladding Process – Role of Location of Injection of Powder Particles

Amitesh Kumar
Department of Mechanical Engineering
National Institute of Technology
Rourkela 769008, India
email: kumar.amitesh.18@gmail.com

Subhransu Roy
Department of Mechanical Engineering
Indian Institute of Technology Kharagpur
Kharagpur 721302, India
email: suroy@iitkgp.ac.in

Abstract

A two-dimensional heat transfer model is developed to study the role of the location of injection of powder particles in to the melt pool stirred by convection due to thermocapillary force during the powder blown laser cladding process. The effects of both positive and negative surface tension coefficients and the absorbed laser power are studied. For the positive surface tension coefficients the powder is injected in a region where the flow velocity is in the direction of powder injection velocity and therefore the particles travel a little deeper into the melt pool. For negative surface tension coefficients the powder is injected in a region where the flow in opposite to the direction of injection velocity and the particles always stay very close to the melt pool surface. To solve the discretized governing equations finite volume method in a multiblock non-orthogonal grid system with collocated primitive variable approach is utilized.

NOMENCLATURE

a	fraction of lower mode in the laser beam
b	deposition width (m)
c_p	specific heat (J/kg K)
$\mathbf{F}$	irradiation flux vector (W/m^2)
f_l	liquid fraction
H_c	built-up height (m)
H_s	substrate melt depth (m)
h	specific sensible enthalpy (J/kg)
h_c	heat transfer coefficient (W/m^{2}K)
h_{max}	maximum pool specific sensible enthalpy (K)
h_p	specific powder preheat (J/kg)
$\hat{\mathbf{i}}, \hat{\mathbf{j}}, \hat{\mathbf{k}}$	unit vectors along x, y & z axis
k	thermal conductivity (W/m K)
$\dot{m}_p$	powder deposition rate (kg/s)
$\hat{\mathbf{n}}$	unit surface normal vector
P	laser power (W)
p	dynamic pressure (N/m^2)
$\dot{q}_h'''$	volumetric energy source (W/m^3)
R	radius of curvature (m)
r_p	radius of powder particle (m)
r_0	radius of Gaussian laser beam (m)
Ste	Stefan number
T	temperature (K)
t	time (s)
U	scanning speed (m/s)
V_s	velocity of the solidification front (m/s)
$\mathbf{v}$	velocity vector (m/s)
y_{top}	Untreated substrate height
x, y, z	Cartesian coordinate system
α	thermal diffusivity (m^2/s)
Δh_{sl}	specific latent heat of fusion (J/kg)
ΔP_{IZ}	power absorbed by powder (W)
$\Delta \mathcal{V}_m$	volume of the melt pool (m^3)
ϵ	emissivity
η	fractional absorption of laser power
μ	dynamic viscosity (kg/m s)
ρ	density of the medium (kg/m^3)
σ	surface tension (N/m)
σ_b	Stefan Boltzmann constant (W/m^{2}K^4)

Subscript

$_0$	reference
∞	ambient condition
l	liquidus
S	solidus

Superscript

$\star$	dimensionless

INTRODUCTION

Laser cladding with powder feed is one of the emerging technologies having multiple applications such as coating, tools repair, rapid prototyping, manufacturing of functionally graded materials. The basic working principle laser cladding with powder feed is melting a substrate surface by a moving laser beam and adding pneumatically delivered metal/ceramic powders into the melt pool, which subsequently melts and forms a coating layer over the substrate. That is, the process involves (i) interaction of powder particles with the laser beam, (ii) interaction of powder particles with the molten pool and (iii) the development of built-up layer over the substrate. Despite numerous advantages of this process, its industrial applications are still limited due to the complex relationship among the process parameters (i.e. laser power, process speed etc.) and the process characteristics (i.e. clad geometry, morphology of the clad layer etc.).

Basically, there are two main objectives of developing a heat transfer model of the laser cladding process — (a) prediction/control of build-up geometry and (b) prediction/control of metallurgical characteristics. The geometrical predictions are directly related with the dimensional accuracy of the repair work for degraded mechanical components and building up three-dimensional objects; whereas metallurgical predictions are linked with mechanical properties of the build-up material.

There are several analytical and numerical studies on surface melting, welding and cladding with laser or other sources of energy in the literature [1–3]. These are very useful articles in developing models of several thermal processes and studying temperature profile, melting-solidification, melt pool convection *etc.* There are a few articles dealing with the role of powder feed parameters on the build-up geometry and its properties during cladding [4–8]. These articles only deal with the total power feed rates but does not capture the role of the location of injection point of powder particles on the molten surface and effect of the initial diameter of the injected powder particles. Recently the thermal dynamics of melting of solid spherical particles in a melting pool of the same material was studied[9, 10]. Here the role of the location of injection point of powder particles on the molten surface and effect of the initial diameter of the injected powder particles are studied

The governing equation along with boundary conditions are normalized using appropriate scales. The dimensionless governing equation is solved by finite volume method in a non-orthogonal grid system with collocated variable arrangement [11]. The melt pool boundary line on the substrate is tracked iteratively and the build-up layer geometry is constructed over the melt pool [12].

MATHEMATICAL AND NUMERICAL MODELING

Model Description

Fig. 1 shows a schematic diagram of the powder injection into the melt pool during coaxial laser cladding process. The powder particles after absorbing some of the energy from the laser during its flight get heated up to a temperature which may or may not be able to melt the particles completely. These heated up powder particles then pierce the free surface of the molten pool and go inside. The powder particles are carried away by the convection current inside the pool. During its movement inside the pool the particles get heated by the melt pool and become liquid.

Here the laser beam is assumed to be a mixture of the first two fundamental modes, 40% TEM00 and 60% TEM01*, which gives a near top-hat beam profile [13]. Powder particles get heated up by absorption in the laser-powder interaction zone, termed as *preheating*, The power ΔP_{IZ} is absorbed for preheating the powder of deposition rate $\dot{m}_p$ up to the enthalpy level h_p. The volume fraction of the solid particles in the gas-powder stream is usually very small ($< 1\%$). The intensity profile nature of the attenuated beam is assumed to be invariant. The efficiency parameter η has been introduced to account for the loss by reflection from the irradiated substrate surface as well as for the energy loss due to scattering by powder particles. The absorbed power ηP is responsible for heating up the powder particles and the substrate (i.e. if ΔP_{IZ} is the amount of power required in preheating of the powder particles, then substrate will receive only $(\eta P - \Delta P_{IZ})$ amount of power). Preheated powder enters the melt pool with a velocity $\mathbf{v}_{pn}$ (whose magnitude depends on the powder mass flow rate $\dot{m}_p$, particle loading in the gas-powder stream and the area of the window of the melt pool free surface through which particles are entering into the melt pool) in a direction normal to the melt pool free surface.

Governing Equations

The laser source is moving with a constant speed U in the negative x direction with respect to the substrate. However, transport phenomena occurring inside the molten pool can be conveniently modeled with respect to a coordinate system attached to the moving laser source, thus, reducing it to a quasi-stationary process in the Eulerian reference frame where the substrate moves with constant speed U in the x-direction. A one-dimensional beam intensity profile which varies only in the x-direction is considered because of the rapid back-and-forth movement of the laser source in a plane perpendicular

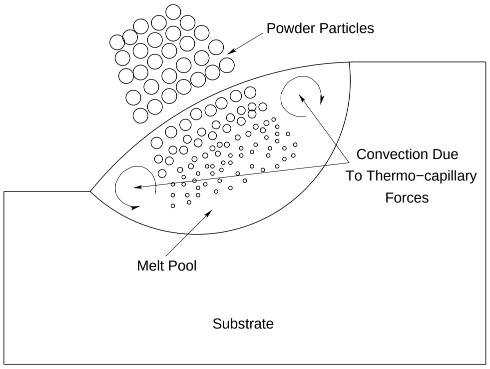

Figure 1: A Schematic diagram of the powder injection into the melt pool

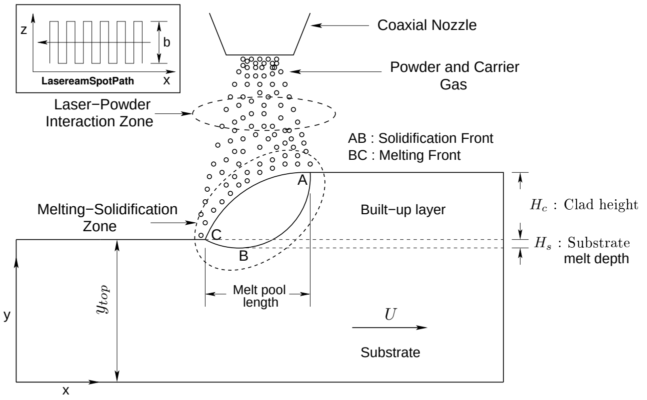

Figure 2: Schematic diagram of coaxial blown powder laser cladding process

to the $x-y$ plane (see Fig. 2) and the problem reduces to two dimensions. The governing equations of continuity, momentum and energy in the moving coordinate system for the domain containing incompressible liquid in the molten pool and heated solid in the surrounding region is expressed as follows:

Conservation of mass and linear momentum (Navier-Stokes) equations:

$$\nabla\cdot(\rho\mathbf{v}) = 0 \tag{1}$$

$$\frac{\partial(\rho u)}{\partial t}+\nabla\cdot(\rho\mathbf{v}u) = -\frac{\partial p}{\partial x}+\nabla\cdot(\mu\nabla u)+\dot{q}_u''' \tag{2}$$

$$\frac{\partial(\rho v)}{\partial t}+\nabla\cdot(\rho\mathbf{v}v) = -\frac{\partial p}{\partial y}+\nabla\cdot(\mu\nabla v)+\rho g\beta(T-T_0)+\dot{q}_v''' \tag{3}$$

where g is the gravitational acceleration and T_0 is the reference temperature which is taken to be equal to the liquidus temperature T_l of the substrate. The volumetric sources for the momentum (u and v) equations are :

$$\dot{q}_u''' = \underbrace{\left[\dot{m}_{fs}'''(u_p-u)\right]}_{\text{Part-I}}+\underbrace{A(u-U)}_{\text{Part-II}} \tag{4}$$

$$\dot{q}_v''' = \underbrace{\left[\dot{m}_{fs}'''(v_p-v)\right]}_{\text{Part-I}}+\underbrace{Av}_{\text{Part-II}} \tag{5}$$

In the above Eqs. (4) and (5), 'Part-I' is due to mass addition into the melt-pool according to the model description. For these equations 'Part-I' is non-zero only for the control volumes neighboring free surface boundary through which powder particles are entering into the pool. Accordingly the mass source strengths are defined as :

$$\dot{m}_{fs}''' = \dot{m}_p''\frac{\Delta S_{fs}}{\Delta\Omega_{fs}},\quad \dot{m}_p'' = \frac{\dot{m}_p'}{\Sigma\Delta S_{fs}},\quad \dot{m}_p' = \frac{\dot{m}_p}{b} = \rho U H_c \tag{6}$$

In Eq. (6) $\Delta\Omega_{fs}$ is the volume of the cell having free surface boundary of area ΔS_{fs} through which powder particles are entering with mass flux $\dot{m}_p''$ assumed uniform over the whole particle injection window area of $\Sigma\Delta S_{fs}$.

'Part-II' of Eqs. (4) and (5) originates from the phase changing part between completely solid and liquid phase, which offers resistance towards fluid flow in that region. In the standard porosity-enthalpy formulation for a melting-solidification problem this resistance can be conveniently formulated using Darcy's model for porous media in conjunction with the Carman-Koseny relationship as reported by Voller and Prakash [14]

$$\mathbf{grad}\,p = \frac{-C_0(1-f_l)^2}{f_l^3}\mathbf{v} \tag{7}$$

This equation suggests the following form for the function A in Eqs. (4) and (5)

$$A = \frac{-C_0(1-f_l)^2}{f_l^3} \tag{8}$$

The value of C_0 depends on the morphology of the porous media. In the current study C_0 is assumed to be a constant and set to 1.016×10^6kg/s m^3 [15]. f_l is the liquid fraction.

Conservation of energy

$$\frac{\partial(\rho h)}{\partial t}+\nabla\cdot(\rho\mathbf{v}h) = \nabla\cdot(\rho\alpha\nabla h)+\dot{q}_h''' \tag{9}$$

The heat source $\dot{q}_h'''$ is zero in the solid region ($h<h_S$) and elsewhere it is defined as,

$$\dot{q}_h''' = \underbrace{\dot{\rho_s}\left[h_p-(h+\Delta h_{sl})\right]}_{\text{Part-I}}-\underbrace{\left[\frac{\partial(\rho\Delta h_{sl}f_l)}{\partial t}+\nabla\cdot(\rho\mathbf{v}\Delta h_{sl}f_l)\right]}_{\text{Part-II}} \tag{10}$$

In Eq. (10), $\dot{\rho_s}$ is the powder melting rate per unit volume which is a function of the local temperature of the molten pool. The calculation of $\dot{\rho_s}$ is given in the appendix.

'Part-I' in Eq. (10) is due to heating and melting of the solid powder mass injected into the melt pool according to the model assumption and 'Part-II' is due to conversion of latent enthalpy to sensible enthalpy at the solidification interface and vice-verse at the melting interface [14]. Due to the extended range of melting temperature for an alloy, specific latent heat is assumed to be linearly proportional to the liquid fraction f_l. Among the various models of liquid fraction, linear function of sensible heat has been adopted for this simulation,

$$h\geq h_l : f_l = 1.0,\quad h_S<h<h_l : f_l = \frac{h-h_S}{h_l-h_S},\quad h\leq h_S : f_l = 0 \tag{11}$$

The Boundary Conditions.

The laser beam is assumed to be a mixture of the first two fundamental modes, 40% TEM00 and 60% TEM01*, which is having near top hat beam profile. The combined intensity profile for a mixed mode laser beam is given by [13],

$$\mathbf{F} = \sqrt{\frac{8}{\pi}}\frac{1}{(1+a)r_0}\left[\frac{\eta P - \Delta P_{IZ}}{b}\right]\left[a + (1-a)\frac{2x^2}{r_0^2}\right] e^{(-2x^2/r_0^2)}\hat{\mathbf{j}} \tag{12}$$

$$\text{where} \quad \Delta P_{IZ} = b\dot{m}'_p(h_p - h_\infty) \tag{13}$$

In Eq. (12), a is the fraction of the lower mode. The efficiency parameter η accounts for the energy loss due to scattering/reflection by powder particles and loss by reflection from the irradiated surface and ΔP_{IZ} is the power absorbed in preheating the powder up to enthalpy level h_p in the laser-powder interaction zone. During material addition for building a surface layer, a curved free melt surface is formed that connects the untreated substrate surface to the built-up layer. The shape of this free surface is derived from the balance of all the normal forces at liquid-gas interface. The present static equilibrium model adopted is an approximate one. The boundary conditions on this top surface and far away from it are:

Top surface

$$\text{Shape} \quad : \quad x \le x_C : y = y_{top},\ x \ge x_A : y = y_{top} + H_c,$$

$$x_A < x < x_C \quad : \quad \frac{\sigma}{R} + 2\mu\frac{\partial \mathbf{v}}{\partial n}\cdot\hat{\mathbf{n}} = p - p_\infty \tag{14}$$

$$+\rho g(H_c + y_{top} - y) \tag{15}$$

$$\text{Momentum} \quad : \quad \mu\frac{\partial \mathbf{v}}{\partial n}\cdot\hat{\mathbf{s}} = \frac{\partial \sigma}{\partial s}\hat{\mathbf{s}}\cdot\hat{\mathbf{s}} \tag{16}$$

$$\text{Energy} \quad : \quad \mathbf{F}\cdot\hat{\mathbf{n}} = -\hat{\mathbf{n}}\cdot(\rho\alpha\nabla h) + h_c(T - T_\infty) \tag{17}$$

$$+\epsilon\sigma_b(T^4 - T_\infty^4) \tag{18}$$

Other surfaces (far from the hot spot)

$$\text{Momentum} \quad : \quad x \to \pm\infty, y \to -\infty : u = U,\ v = 0 \tag{19}$$

$$\text{Energy} \quad : \quad x \to -\infty,\ y \to -\infty : h = h_\infty, \tag{20}$$

$$x \to \infty : \frac{\partial h}{\partial x} = 0 \tag{21}$$

Powder Particle Melting Model (Governing Equations)

The equation for the conservation of mass of solid powder particles is

$$\frac{\partial \rho_s}{\partial t} + \nabla\cdot(\mathbf{v}\rho_s) \quad = \quad \dot{\rho}_s \tag{22}$$

where ρ_s is the mass of the solid per unit volume of the mixture of solid and liquid, $\dot{\rho}_s$ is the rate of depletion of the solid mass per unit volume due to melting and $\mathbf{v}$ is the surrounding fluid velocity. It has been assumed that the solid particles are moving with the same velocity as the surrounding fluid velocity, i.e., there is no slip between the solid particles and the surrounding liquid. When a metal spherical particle at its melting temperature is subjected to a surrounding superheated melt pool of its own liquid the melting commences and with the passage of time the mass of the solid decreases until it melts completely to liquid. The rate of melting of the solid particle in terms of the decrease of solid mass per unit volume $\dot{\rho}_s$ depends on the superheat of the surrounding melt as explained by [10].

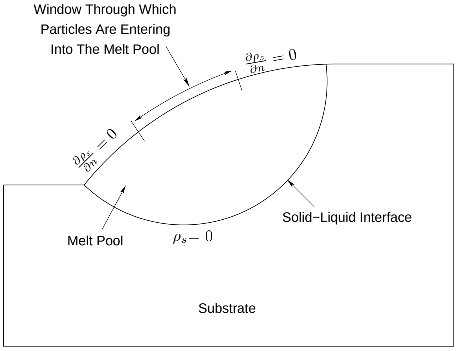

Figure 3: Boundary condition for the powder particles

Similarly, we can also write the equation for liquid as

$$\frac{\partial \rho_l}{\partial t} + \nabla\cdot(\mathbf{v}\rho_l) \quad = \quad \dot{\rho}_l \tag{23}$$

Since $\rho_s + \rho_l = \rho$ and $\dot{\rho}_s + \dot{\rho}_l = 0$, adding equations (22) and (23) gives the well known continuity equation in the following form

$$\frac{\partial \rho}{\partial t} + \nabla\cdot(\mathbf{v}\rho) \quad = \quad 0 \tag{24}$$

Powder Particle Melting Model (Boundary conditions)

Fig. 3 shows the boundary condition for the powder particles that are injected into the molten pool through the powder injection window. It has been assumed that the powder particles are melting completely within the melt pool before reaching the solid-liquid interface. This assumption is quite reasonable as the powder particles are fed around the location of maximum pool temperature. Also, we have considered same material for the substrate and the powder particles. The mass of the incoming powder particles through the powder injection window is incorporated into the model as the surface flux and is assumed uniform for the entire area of the particle injection window. The powder particles are conveyed by carrier gas and the loading is only 1%, therefore the particle velocity v_p to achieve powder mass flow rate of over injection area of S_{sf} is given by

$$v_p \quad = \quad \frac{\dot{m}'_p}{0.01\,\rho\,S_{sf}}$$

The solid concentration near the surface after injection into the melt pool at a mass flow rate of $\dot{m}'_p$ through a surfer area of S_{sf} is determined by the rate by which the solid particles are carried away by the surrounding molten liquid. A Neumann boundary condition is applied at the remaining part of the free surface as shown in the figure 3.

Non-dimensional governing equations

The beam spot radius, r_0, is a controllable laser parameter and is a natural choice for characteristic length. Among the various possibilities speed of thermal diffusion ($U_0 = \alpha_0/r_0$) has been chosen as velocity scale due to its universality and relatively small dimensions of the melt pool with respect to the bulk solid substrate. The dimensionless parameters are listed below.

$$\rho^\star = \frac{\rho}{\rho_0}, \alpha^\star = \frac{\alpha}{\alpha_0}, \mu^\star = \frac{\mu}{\mu_0}, \mathbf{r}^\star = \frac{\mathbf{r}}{r_0}, \boldsymbol{\nabla}^\star = r_0\boldsymbol{\nabla},$$

$$t^\star = \frac{U_0 t}{r_0}, \mathbf{v}^\star = \frac{\mathbf{v}}{U_0}, U^\star = \frac{U}{U_0}, H_c^\star = \frac{H_c}{r_0}, p^\star = \frac{p}{\rho_0 U_0^2},$$

$$P^\star = \frac{\eta P}{\rho_0\alpha_0(h_l - h_\infty)r_0}, \dot{m}'''^\star_{fs} = \dot{m}''^\star_p \frac{\Delta S^\star_{fs}}{\Delta\Omega^\star_{fs}},$$

$$\dot{m}''^\star_p = \frac{\dot{m}^\star_p}{\Sigma\Delta S^\star_{fs}}, \dot{m}'''^\star_m = \frac{\dot{m}^\star_p}{\Delta\mathcal{V}^\star_m}, T^\star = h^\star,$$

$$h^\star = \frac{h - h_\infty}{h_l - h_\infty}, T^\star = \frac{T - T_\infty}{T_l - T_\infty}, \mathrm{Ste} = \frac{h_l - h_\infty}{\Delta h_{sl}},$$

$$\mathrm{Ma} = \frac{d\sigma}{dT}\frac{(h_l - h_\infty)r_0}{c_{p0}\mu_0\alpha_0}, \mathrm{Pr} = \frac{\mu_0}{\rho_0\alpha_0}, \mathrm{Bi} = \frac{h_c r_0}{k},$$

$$\mathrm{Ra} = \frac{\rho_0 g\beta(T_l - T_\infty)r_0^3}{\mu_0\alpha_0}, \mathrm{We} = \frac{\rho_0 U_\sigma^2 r_0}{\sigma},$$

$$\mathrm{Bd} = \frac{\rho_0 g r_0^2}{\sigma}, \mathrm{Ca} = \frac{\mu_0 U_\sigma}{\sigma}, \mathrm{N}_c = \frac{k}{\epsilon\sigma_b(T_l - T_\infty)^3 r_0}$$

It is to be noted here that for a constant specific heat value c_p dimensionless specific enthalpy $h^\star$and dimensionless temperature $T^\star$ are same. The governing equations for the cladding model are normalized using the above dimensionless variables and parameters.

Nondimensionalization of the governing equation (22) for powder particles have been done using the normalizing variables and parameters consistent with the cladding model.

The governing equation (22) is normalized using the properties of the liquid iron at its liquidus temperature as reference properties (*i.e.* ρ_0, α_0, k_0, c_{p0}, *etc.*); the radius of the Gaussian component in the laser beam r_0 as the length scale and the speed of thermal diffusion ($U_0 = \alpha_0/r_0$) as the velocity scale. The dimensionless parameters are:

$$\rho_s^\star = \frac{\rho_s}{\rho_0}, \tau = \frac{\alpha_0 t}{r_L^2}, \mathbf{v}^\star = \frac{\mathbf{v}}{U_0}$$

The dimensionless governing equation can be written as

$$\frac{\partial\rho_s^\star}{\partial\tau} + \nabla^\star\cdot(\mathbf{v}^\star\rho_s^\star) \quad = \quad \dot{\rho_s}^\star \qquad (25)$$

The dimensionless rate of melting of the solid particle in terms of the decrease of dimensionless solid mass per unit volume $\dot{\rho_s}^\star$ depends on the Stefan number Ste of the surrounding melt.

Table 1: Properties of liquid iron and other values used [16, 17]

ρ	$7.03\times10^3\,kg/m^3$	σ	$1.8\,N/m$
C_p	$824\,J/kg\,K$	$d\sigma/dT$	$-0.43\times10^{-3}\,N/m\,K$
k	$36\,W/m\,K$	$h_l - h_\infty$	$1050\times10^3\,J/kg$
α	$6.2\times10^{-6}\,m^2/s$	T_l	1538^oC
μ	$5.6\times10^{-3}\,kg/m\,s$	Δh_{sl}	$247\times10^3\,J/kg$
β	$1.22\times10^{-4}\,1/K$	h_c	$250\,W/m^2\,K$
ϵ	0.19	σ_b	$5.67\times10^{-8}\,W/m^2\,K^4$
r_L	$1.0\,mm$	r_p	$100\,\mu m$ or $150\,\mu m$

As explained by [10] it can be shown that $\dot{\rho}_s^\star = -B\rho_s^\star$ where $B = 9.8\,(h^\star - 1)\,\mathrm{Ste}$.

The dimensionless governing equations are discretized and solved in a multiblock non-orthogonal grid system by finite volume method with collocated variable arrangement [11]. The melt pool boundary line on the substrate is tracked iteratively and the built-up layer geometry is constructed over the molten part of the substrate.

RESULTS AND DISCUSSION

The thermo-physical properties of liquid iron at melting temperature and other values, listed in Table 1, are used for this simulation. In this simulation, dimensionless input parameters, which are kept fixed for the entire study, are chosen as $h_p^\star = 1.0$, $h_S^\star = 0.95$, the value of the fraction of lower mode $a\,(= \mathrm{TEM00}/(\mathrm{TEM00} + \mathrm{TEM01}^\star))$ is taken equal to 0.4 and $\mathrm{Ra} = 3.0\times10^2$. It has been shown recently by Kumar and Roy [6] that Rayleigh number does not have much effect on the clad characteristics. Usually pure liquid metals have negative temperature gradient of surface tension ($d\sigma/dT < 0$), but the small amount of surface-active elements like sulfur and manganese makes the surface tension to increase with the increase in temperature, indicating a positive surface tension gradient ($\partial\sigma/\partial T > 0$) [16, 18] and therefore the effect of both positive and negative Marangoni numbers (2×10^3 and -2×10^3) on the clad characteristics is presented in this article. The center of the laser beam is fixed at the location $x^\star = 6.0$ for all of the test cases and its radius is taken as $1mm$. The powder particles of diameter $200\,\mu m$ are conveyed by carrier gas with 1% loading. Powder particles of diameter $200\,\mu m$ and laser beam radius of $1mm$ corresponds to dimensionless powder radius of $r_p^\star = 0.1$.

Melt pool characteristics

Figure 4 shows the streamlines (top) and the specific sensible enthalpy contours (bottom) in the melt pool for a positive surface tension gradient represented by Ma=2.0×10^3 for power deposited per unit length of travel ($P'^\star/U^\star$) equal to 4, powder deposited per unit length of travel ($\dot{m}_p'^\star/U^\star$) equal to 0.2 and a scanning speed of $U^\star$=1.0. The melt pool is bounded by the sensible enthalpy contour lines having values in the range 1.00 to 0.95; these ranges denote the mushy region across which

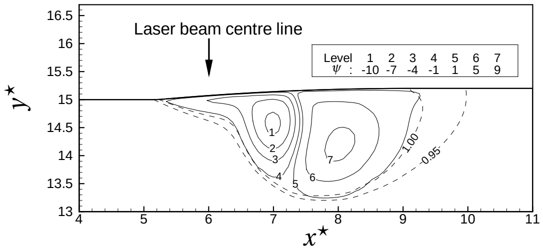

(a) Streamlines

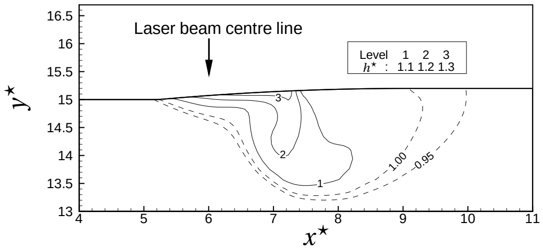

(b) Isoenthalpy lines

Figure 4: Streamlines, Isoenthalpy and powder concentration lines in the melt pool for Ma = 2.0×10^3 $P'^\star/U^\star = 4.0$, $\dot{m}_p'^\star/U^\star = 0.2$ $P'^\star = 4.0$, $\dot{m}_p'^\star = 0.2$, $U^\star = 1.0$ and $r_p^\star = 0.1$ ($\psi > 0$ is anticlockwise cell)

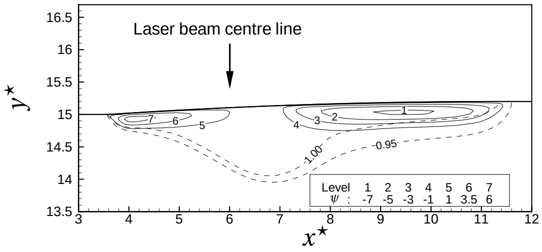

(a) Streamlines

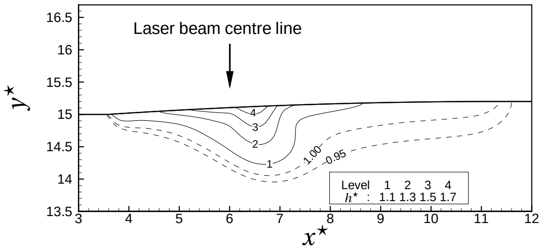

(b) Isoenthalpy lines

Figure 5: Streamlines, Isoenthalpy and powder concentration lines in the melt pool for Ma = -2.0×10^3 $P'^\star/U^\star = 4.0$, $\dot{m}_p'^\star/U^\star = 0.2$ $P'^\star = 4.0$, $\dot{m}_p'^\star = 0.2$, $U^\star = 1.0$ and $r_p^\star = 0.1$ ($\psi > 0$ is anticlockwise cell)

phase change takes place between liquid and solid. In the melt pool the sensible enthalpy contours having values of 1.1 and above are shown. Somewhere in the middle of the melt pool surface the temperature reaches a peak and it decreases towards the melt pool boundary. Powder of particle radius 0.1 is injected into the melt pool through the powder injection window whose width is chosen to be equal to the radius of the laser beam. The temperature peak falls within this injection window. Surface tension change with temperature causes net force on the surface that drives the convection in the melt pool. For positive surface tension gradient the surface flow from upstream and downstream direction converges towards a stagnation zone on the surface and then it turns in the downward direction forming a central vertical jet between two contra-rotating cells. The velocity of recirculation reaches values that are one order of magnitude higher than the scanning speed of the laser. The upstream recirculating cell is smaller than the downstream recirculating cell. In Fig. 4a the strength of the upstream clockwise cell is -10 and the strength of the downstream anticlockwise cell is 9 indicating that the smaller upstream cell experiences stronger convection current compared to the downstream cell. The downstream cell experiences an almost uniform temperature in its upper region and the temperature variation is mostly confined to the upstream cell region over which the laser beam falls.

Figure 5 shows the streamlines (top) and the specific sensible enthalpy contours (bottom) in the melt pool for the same set of input parameters *i.e.*, scanning speed $U^\star$ of 1.0 keeping the $P'^\star/U^\star$ =4.0 and ($\dot{m}_p'^\star/U^\star$) equal to 0.2, but for a negative surface tension gradient, i.e., Ma=-2×10^3. The melt pool length is increased considerably and it becomes shallower compared to the melt pool for positive surface tension gradient (see Fig. 4). As the surface tension increases with the decrease in temperature towards the boundary of the melt pool surface, the molten metal at the surface flows outward in opposite directions (upstream and downstream) from the location of maximum melt pool temperature to form two counter-rotating cells; there is a stagnant region with very slow vertical velocity (less than the scanning speed) separating these two counter-rotation cells. As the melt pool length elongates for the negative Ma the surface temperature gradient reduces and the strength of the recirculating cell also reduces.

Powder transport characteristics

For positive Ma the powder particles are injected into the melt pool surface above the upstream recirculating cell. This added material is dragged down by the central vertical jet in the molten pool. The powder concentration contours in Fig 6 top for powder radius of 0.1 showing lowest value of 0.0002 and highest value of 0.01 reveal that the powder melts very close to the surface. There is a spike in the 0.0002 concentration contour due to the central jet flow. The powder is injected over a length of one laser-radius r_0 and the solid concentration decreases from 0.01 to 0.0002 over a distance of 0.15 along the jet. In must be noted that in the surface region where the powder is injected the surface forces due to surface tension, that is usually responsible for the surface flow, is neglected. Figure 6 mid-

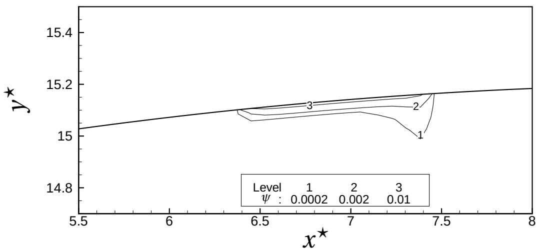

(a) $r_p^\star = 0.1$, $\mathrm{Ma} = 2.0 \times 10^3$

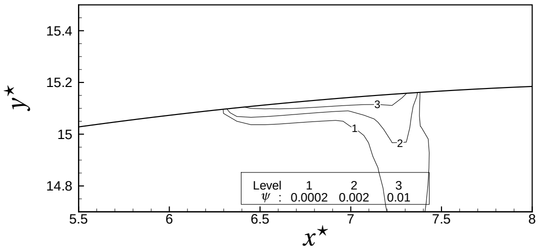

(b) $r_p^\star = 0.15$, $\mathrm{Ma} = 2.0 \times 10^3$

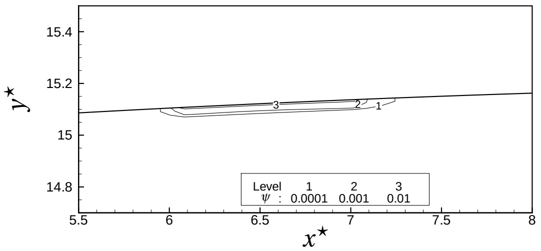

(c) $r_p^\star = 0.1$, $\mathrm{Ma} = -2.0 \times 10^3$

Figure 6: Powder concentration lines in the melt pool for $P'^\star/U^\star = 4.0$, $\dot{m}_p'^\star/U^\star = 0.2$, $U^\star = 1.0$ for different powder radius

dle shows the powder concentration contours for injection of larger sized powder of radius 0.15. It is observed that the solid concentration along the jet reduces from 0.002 to 0.0002 over a distance of 0.4.

Figure 6 bottom shows that for negative Ma the powder with particle radius of 0.1 is injected through the melt pool surface above the stagnant region which experiences the maximum surface temperature and this injected material is dragged away by the surface flow. There is significant conduction heat transfer in the downward direction in this stagnant region, as evidenced by the sensible enthalpy contours shown in Fig. 5(b), making the melt pool deep in this stagnant region. The powder concentration contours showing a minimum value of 0.0001 and a maximum value of 0.01 reveal that the powder melts very near the region of injection on the surface. The melt pool temperature is maximum on the surface in this region and decreases away from it.

Figures 7 and 8 show the extent of significant powder concentration in the melt pool. The powder is injected at the center of the melt pool surface over a window of one laser radius and the concentration contour lines reveal that the powder melts very close to the surface. For the positive Ma shown in Fig. 7 the powder is injected in a region where the flow velocity is in the direction of powder injection velocity and therefore the concentration having 0.02 value protrudes a little deeper into the melt pool like a spike for power level of 4.0 and this spike shifts inside the melt pool as the powder deposition rate

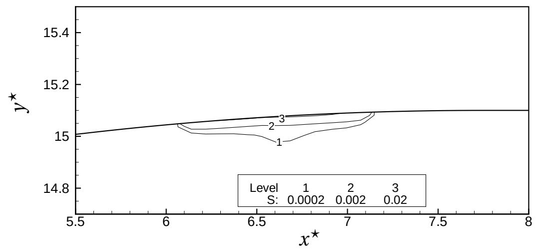

(a) $P'^\star = 4.0$, $\dot{m}_p'^\star = 0.2$ and $U^\star = 2.0$

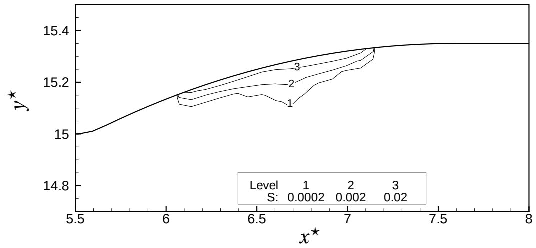

(b) $P'^\star = 4.0$, $\dot{m}_p'^\star = 0.7$ and $U^\star = 2.0$

Figure 7: Powder concentration contour lines for $\mathrm{Ma} = 2.0 \times 10^3$, $r_p^\star = 0.1$

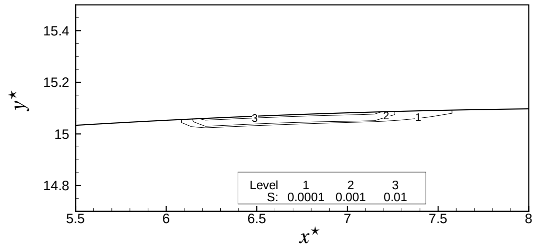

(a) $P'^\star = 4.0$, $\dot{m}_p'^\star = 0.2$ and $U^\star = 2.0$

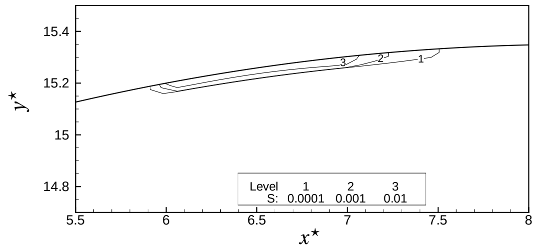

(b) $P'^\star = 4.0$, $\dot{m}_p'^\star = 0.7$ and $U^\star = 2.0$

Figure 8: Powder concentration contour lines for $\mathrm{Ma} = -2.0 \times 10^3$, $r_p^\star = 0.1$

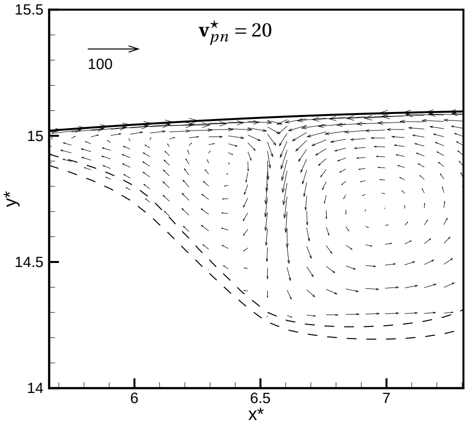

(a) $P'^\star = 4.0$, $\dot{m}'^\star_p = 0.2$ and $U^\star = 2.0$

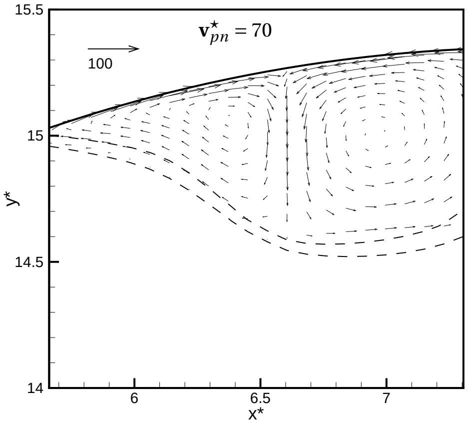

(b) $P'^\star = 4.0$, $\dot{m}'^\star_p = 0.7$ and $U^\star = 2.0$

Figure 9: Vector plots for Ma = 2.0×10^3, $r^\star_p = 0.1$

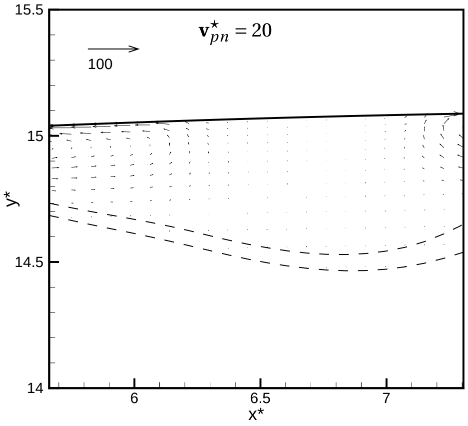

(a) $P'^\star = 4.0$, $\dot{m}'^\star_p = 0.2$ and $U^\star = 2.0$

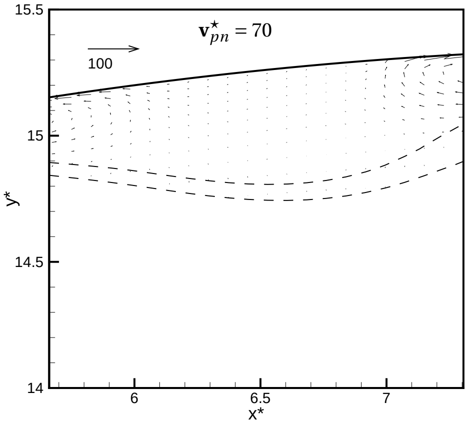

(b) $P'^\star = 4.0$, $\dot{m}'^\star_p = 0.7$ and $U^\star = 2.0$

Figure 10: Vector plots for Ma = -2.0×10^3, $r^\star_p = 0.1$

increases to 0.7. For negative Ma shown in Fig. 8 the powder is injected in a region where the flow is almost stagnant. The concentration contour in the range of 0.01 to 0.0001 is always very close to the melt pool surface even when the powder deposition rate is increased form 0.2 to 0.7

The velocity of the flow near the zone of powder injection is shown in figure 9 and 10. Here,$\mathbf{v}^\star_{pn}$ represents the normal velocity with which powder particles with powder mass flow rate of 0.2 and 0.7 are entering into the melt pool surface close to the region in between six and seven. For positive Ma the melt pool velocity of the central downward jet in between the two recirculation cells becomes as high as 25 but for negative Ma the central upward jet in between the recirculation cells has a velocity less that 1 making the melt pool almost stagnant in that region.

CONCLUSIONS

A computer simulation code for laser cladding has been developed. For particular laser power, scanning speed and powder flow rate the simulation results of melt flow, temperature and powder concentration in the melt pool for positive and negative surface tension gradients have been presented for laser beam radius of 1mm and powder particle radius of $200\mu m$ injected at the center of the melt pool. The results are presented in dimensionless form. For positive surface tension gradients the added material is dragged down by the central vertical jet in the molten pool. The solid powder melts very close to the pool surface. For positive surface tension gradients the added material falls in the stagnant region and is dragged away towards the periphery of the melt pool by the surface flow.

REFERENCES

[1] G M Oreper and J Szekely. Heat and fluid-flow phenomena in weld pools. *J Fluid Mech*, 147:53–79, 1984.

[2] A P Mackwood and R C Crafer. Thermal modelling of laser welding and related processes : a literature review. *Optics & Laser Technology*, 37:99–115, 2005.

[3] B Xiao and Y Zhang. Marangoni and buoyancy effects on direct metal laser sintering with a moving laser beam. *Numerical Heat Transfer, Part A: Applications*, 51(8):715–733, January 2007.

[4] A F A Hoadley and M Rappaz. A thermal model of laser cladding by powder injection. *Metall. Trans. B*, 23B:631–42, 1992.

[5] A Fathi, E Toyserkani, A Khajepour, and M Durali. Prediction of melt pool depth and dilution in laser powder deposition. *Journal of Physics D: Applied Physics*, 39:2613–2623, 2006.

[6] Amitesh Kumar and Subhransu Roy. Effect of three-dimensional melt pool convection on process characteristics during laser cladding. *Computational Materials Science*, 46(2):495–506, 2009.

[7] Amitesh Kumar and Subhransu Roy. Development of a theoretical process map for laser cladding using a three-dimensional conduction heat transfer model. *Numerical Heat Transfer, Part A: Applications*, 56(6):478–496, 2009.

[8] U de Oliveira, V Ocelik, and J Th M de Hosson. Analysis of coaxial laser cladding processing conditions. *Surface & Coatings Technology*, 197:127–136, 2005.

[9] Amitesh Kumar and Subhransu Roy. Melting of a solid sphere placed in an infinite medium – effect of forced convection. *Numerical Heat Transfer, Part A: Applications*, 55 (6):594–609, 2009.

[10] Amitesh Kumar and Subhransu Roy. Heat transfer characteristics during melting of a metal spherical particle in its own liquid. *International Journal of Thermal Sciences*, 49 (2):397–408, 2010.

[11] Joel H Ferziger and M Peric. *Computational Methods for Fluid Dynamics*. Springer, third edition, 2002.

[12] S. Kumar, S. Roy, C. P. Paul, and A. K. Nath. Three-dimensional conduction heat transfer model for laser cladding process. *Numerical Heat Transfer, Part B*, 53:271–287, 2008.

[13] R L Philips and C L Andrews. Spot size and divergence for laguerre gaussian beams of any order. *Applied Optics*, 22 (5):643–644, 1983.

[14] V R Voller and C Prakash. A fixed grid numerical modelling methodology for convection-diffusion mushy region phase-change problems. *International Journal of Heat and Mass Transfer*, 30(8):1709–1719, 1987.

[15] X K Lan and J M Khodadadi. Fluid flow, heat transfer and solidification in the mold of continuous casters during ladle change. *International Journal of Heat and Mass Transfer*, 44:953–965, 2001.

[16] Kenneth C Mills. *Recommended values of thermophysical properties for selected commercial alloys*. Woodhead Publishing Limited, Cambridge England, 2002.

[17] Frank P Incropera and David P DeWitt. *Fundamentals of Heat and Mass Transfer*. John Willy & Sons, fifth edition, 2002.

[18] M. J. McNallan and T. Debroy. Effect of temperature and composition on surface tension in Fe-Ni-Cr alloys containing sulfur. *Metallurgical and Materials Transaction B*, 22(4):557–560, 1991.